High-Accuracy Generalized Average Model of Dual Active Bridge Converters

Deshmukh, Rohan Shailesh; Bauer, Pavol; Vahedi, Hani

DOI
10.1109/OJPEL.2024.3382808

Publication date
2024

Document Version
Final published version

Published in
IEEE Open Journal of Power Electronics

IEEE Open Journal of
Power Electronics

Received 11 March 2024; accepted 22 March 2024. Date of publication 28 March 2024;
date of current version 10 April 2024. The review of this article was arranged by Associate Editor Lijun Hang.

Digital Object Identifier 10.1109/OJPEL.2024.3382808

High-Accuracy Generalized Average Model of Dual Active Bridge Converters

ROHAN SHAILESH DESHMUKH (Graduate Student Member, IEEE), PAVOL BAUER (Senior Member, IEEE), AND HANI VAHEDI (Senior Member, IEEE)

Delft University of Technology, 2628CD Delft, The Netherlands

CORRESPONDING AUTHOR: ROHAN SHAILESH DESHMUKH (e-mail: r.s.deshmukh@ tudelft.nl)

This work was supported by the Intelligent Power Electronics (IPE) for High Power Quality of Electricity in Urban Areas with High Fraction of Renewables (IQGRID) project, under Grant TKI1621/1721.

ABSTRACT This article presents a detailed procedure for deriving the generalized average model (GAM) of a dual active bridge converter. The proposed model incorporates higher orders of harmonic components to increase accuracy. Moreover, the turn ratio of the high-frequency transformer (N_t) is considered for realistic modeling, which removes the conventional assumption of unity turn ratio. A detailed model of the DAB will ensure an accurate control design. Required mathematical expressions are derived and explained thoroughly, with an example showcasing a GAM model of the DAB converter up to the ninth harmonics. Several GAM models using different harmonic orders (first, third, fifth, seventh, and ninth harmonics) are derived and compared to the PLECS simulation model and a real-time simulation of the DAB converter on the PLECS RT-Box-2. Results show that including up to the ninth harmonics in the proposed model of the DAB converter leads to achieving accurate voltage and current amplitudes that are almost identical to the simulation outputs and even better than the experimental results.

INDEX TERMS Average model, generalized average model, dual active bridge.

I. INTRODUCTION

Power electronics converters are pivotal in the effective management of energy transfer in renewable energy systems (RES). The application spectrum of power electronic converters is extensive, encompassing electric machine motion control, switched-mode power supplies (SMPS), lighting drive systems, energy storage solutions, distributed power generation, active power filters, flexible AC transmission systems (FACTS), as well as in vehicular and embedded technologies. Control objectives should be defined based on the application [1] to operate a power converter. The foundation for designing these control objectives and for the overall control strategy of a power electronics converter lies in understanding its mathematical modeling. These models are crucial for comprehending, analyzing, and designing power electronics systems. This helps to anticipate performance, refine designs, and devise effective control strategies, ensuring that the converters function optimally within their intended applications. Among the various DC-DC converters, the Dual Active Bridge (DAB) converter has been widely researched in the literature thanks to providing galvanic isolation. Ever since its invention in the early 1990s [2], it has been used in a plethora of applications such as in DC grids [3], [4], [5], [6], [7], [8], [9], Solid State Transformers (SSTs) [10], [11], [12], automotive applications [13], [14], [15], energy storage systems [16], [17], [18], and aerospace [19], [20]. Moreover, this converter topology also exhibits potential within the application of high-power electrolysis [21] and their real-time digital twins [22]. Several mathematical models have been proposed for the DAB converter in the literature. Authors in [23] investigate a 2 kW automotive bidirectional DAB converter to achieve power transfer between a low-voltage port (11V–16 V) and a high-voltage port (240V–450 V). An exact discrete-time small signal model is derived for designing digital control of the converter for different modulation schemes. In [24], a novel average modeling approach for a phase-shift controlled bidirectional DAB converter in the continuous time domain was proposed. The method utilizes switching frequency terms in the Fourier series of the state variables. However, this modeling approach only considers the contribution of the fundamental component for modeling the converter dynamics and transformer current. Three terms (N=0 and N=±1) are considered for the

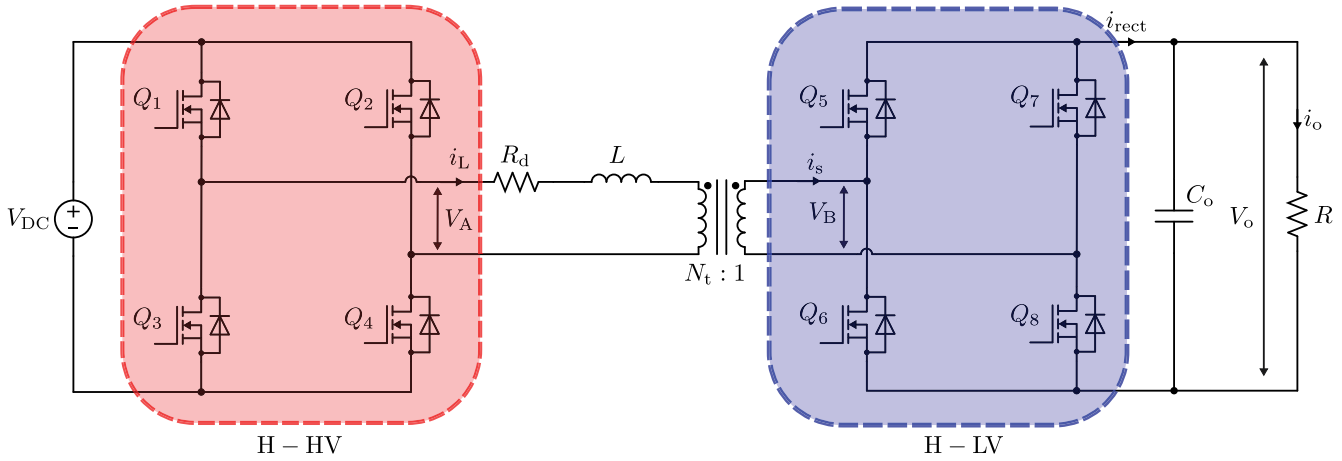

FIGURE 1. Dual Active Bridge Converter.

modeling approach. However, with the contribution of these three terms, a sinusoidal transformer current is obtained, which does not represent the actual current within a DAB converter. Furthermore, only the frequency response of the proposed model has been compared with other modeling approaches. In [25], the average modeling method was applied to general modulation strategies such as dual phase shift (DPS), extended phase-shift (EPS), and triple phase shift (TPS) using the technique proposed in [24]. A method was proposed to minimize the error due to truncating the Fourier series at the fundamental harmonics. Moreover, an additional correction factor was introduced that considers the copper losses in the transformer. A continuous time full-order model retaining high-frequency information of the system was proposed in [26]. A single equation using the Toeplitz operator obtained state equations for every harmonic of a given state variable. Authors in [27] present a method of constructing accurate and scalable models of DC distribution systems containing multiple DAB converters. The reconstruction of DAB transformer currents has been discussed in this work. However, this approach utilizes Fourier and inverse Laplace transformations, making the reconstruction steps complex and challenging to understand.

This work emphasizes DAB converters' Generalized Average Modelling approach, offering additional contributions. Firstly, in the literature, the generalized average modeling of DAB converters does not explain crucial steps within the modeling process. This often creates ambiguity among researchers endeavoring to comprehend this modeling paradigm. To address this gap, the present study delineates an exhaustive, step-by-step methodology to derive the generalized average model of a DAB converter, extending beyond the conventional scope. Moreover, while the GAM methodology frequently presupposes a unity transformer turns ratio for simplification purposes, this assumption does not universally apply to all DAB converter designs. Additionally, the conventional GAM is typically restricted to the fundamental frequency component. Contrasting this, the modeling procedure in this study encompasses the integration of higher-order harmonic elements employing only Fourier transformations and the turns ratio to enhance the model's fidelity and applicability. Furthermore, it provides generalized expressions for more straightforward computation when additional harmonics must be considered. The structure of the paper is as follows: Section II provides an overview of the DAB converter and the concept of generalized average modeling. Section III is the crux of this paper and, therefore, describes the step-by-step proposed modeling procedure for the DAB converter. Results have been illustrated and discussed in Section IV. Finally, conclusions have been provided in Section V.

II. THE DAB CONVERTER AND GAM

A. THE DAB CONVERTER

The DAB converter has been shown in Fig. 1. It consists of two H-bridges, H-HV and H-LV, representing the high-voltage side bridge (leading H-bridge) and the low-voltage side bridge (lagging H-bridge). Depending on the application, each bridge is isolated using a high-frequency (HF) transformer. For this work, the single-phase shift (SPS) strategy has been considered a standard controller in the industry. The expression for the output power of the DAB with the SPS controller is given by,

$$P_o = \frac{(d \cdot (1-d)) \cdot V_{DC} \cdot V_o \cdot N_t}{2 \cdot f_s \cdot L} \tag{1}$$

$$N_t = \frac{V_{DC}}{V_o} \tag{2}$$

$$d = \frac{\phi}{\pi} \tag{3}$$

where P_o is the output power, W. V_o is the output voltage, V. V_{DC} is the input DC voltage, V. f_s is the switching frequency, Hz. N_t is the primary to the secondary turns ratio of the HF transformer. L is the series inductance, H. d is the phase shift duty ratio and, ϕ is the phase angle, rad.

B. CONCEPT OF GENERALIZED AVERAGE MODELLING (GAM)

Most DC-DC converters have only one conversion state, containing only DC variables. The small ripple approximation holds in modeling such converters, wherein the higher-order

TABLE 1. Switching States of the DAB Converter Based on the Switching Functions $S_1(t)$ and $S_2(t)$

Value	Switching States ($S_1(t)$)	Switching States ($S_2(t)$)
+1	Q_1, Q_4 ON	Q_5, Q_8 ON
-1	Q_2, Q_3 ON	Q_6, Q_7 ON

terms are neglected. However, in the case of special DC-DC converters such as the DAB converter, there is an intermediate AC stage, i.e., the intermediate current between the two H-Bridge is purely AC, and therefore, the previously stated small ripple approximation no longer can be applied to such a converter.

To model power electronics converters with more than one conversion stage, the generalized average modeling (GAM) technique can be utilized. This technique captures the contribution of higher-order harmonics using averaging [1]. The GAM is based on the waveform representation using the complex Fourier series [28]. A signal $x(t)$ can be expressed as

$$x(t) = \sum_{-\infty}^{\infty} x_k \cdot e^{jk\omega_s t} \tag{4}$$

where ω_s is the angular switching frequency, rad s^{-1}. x_k is the k^{th} coefficient of variable x which can be defined as,

$$x_k(t) = \frac{1}{T}\int_{t-T}^{T} x(\tau) \cdot e^{-jk\omega_s \tau} d\tau \tag{5}$$

Applying the principle of averaging,

$$x(t) = \langle x \rangle_k(t) \tag{6}$$

GAM technique utilizes two fundamental properties necessary for simplifying the calculations [28]. The first property relates to the derivative of the k^{th} coefficient of variable x.

$$\frac{d\langle x\rangle_k(t)}{dt} = \left\langle \frac{dx}{dt} \right\rangle_k (t) - jk\omega_s \langle x\rangle_k(t) \tag{7}$$

The second property relates to the k^{th} product of two variables x and y,

$$\langle x \cdot y\rangle_k(t) = \sum_i \langle x\rangle_{k-i}(t) \cdot \langle y\rangle_i(t) \tag{8}$$

III. PROPOSED MODELING OF THE DAB CONVERTER

A. STEP 1: DEFINING THE SWITCHING FUNCTIONS

The operation of a DAB converter is mainly governed by two piece-wise switching functions defined as follows:

$$S_1(t) = \begin{cases} +1, & 0 \le t < \frac{T}{2}, \\ -1, & \frac{T}{2} \le t < T \end{cases} \tag{9}$$

$$S_2(t) = \begin{cases} -1, & 0 \le t < \frac{dT}{2}, \\ +1, & \frac{dT}{2} \le t < \frac{dT}{2} + \frac{T}{2} \\ -1, & \frac{dT}{2} + \frac{T}{2} \le t < T \end{cases} \tag{10}$$

Table 1 showcases the switching states of the DAB converter based on the defined piece-wise switching functions where $S_1(t)$ represents the switching function associated with H-HV, and $S_2(t)$ represents the switching function associated with H-LV. For this work, d represents the phase shift duty ratio of H-LV with respect to H-HV.

B. STEP 2: IDENTIFYING THE FOURIER COEFFICIENTS

Any signal $x(t)$ can be defined using a series of sinusoids with the help of Fourier Series [29],

$$x(t) = A_0 + \sum_{n=1}^{N} A_n \cos(n\omega_s t) + \sum_{n=1}^{N} B_n \sin(n\omega_s t) \tag{11}$$

where

$$A_0 = \frac{1}{T}\int_0^T x(t)dt$$

$$A_n = \frac{2}{T}\int_0^T x(t)\cos(n\omega_s t)dt$$

$$B_n = \frac{2}{T}\int_0^T x(t)\sin(n\omega_s t)dt$$

Before analyzing the switching functions, it is evident from preliminary inspection of their definitions that the DC component for both switching functions, $S_1(t)$ and $S_2(t)$ is zero.

1) ANALYSIS OF $S_1(t)$

$$A_n = \frac{2}{T}\left(\int_0^{\frac{T}{2}} \cos(n\omega_s t)dt + \int_{\frac{T}{2}}^{T} -\cos(n\omega_s t)dt\right)$$

$$B_n = \frac{2}{T}\left(\int_0^{\frac{T}{2}} \sin(n\omega_s t)dt + \int_{\frac{T}{2}}^{T} -\sin(n\omega_s t)dt\right)$$

$$A_0 = 0 \tag{12}$$

$$A_n = 0, \ \forall\ n \tag{13}$$

$$B_n = \begin{cases} \frac{4}{n\pi}, & n \text{ is odd} \\ 0, & n \text{ is even} \end{cases} \tag{14}$$

2) ANALYSIS OF $S_2(t)$

$$A_n' = \frac{2}{T}\left(\int_0^{\frac{dT}{2}} -\cos(n\omega_s t)dt + \int_{\frac{dT}{2}}^{\frac{dT}{2}+\frac{T}{2}} \cos(n\omega_s t)dt + \int_{\frac{dT}{2}+\frac{T}{2}}^{T} -\cos(n\omega_s t)dt\right)$$

$$B_n' = \frac{2}{T}\left(\int_0^{\frac{dT}{2}} -\sin(n\omega_s t)dt + \int_{\frac{dT}{2}}^{\frac{dT}{2}+\frac{T}{2}} \sin(n\omega_s t)dt + \int_{\frac{dT}{2}+\frac{T}{2}}^{T} -\sin(n\omega_s t)dt\right)$$

$$A_0' = 0 \tag{15}$$

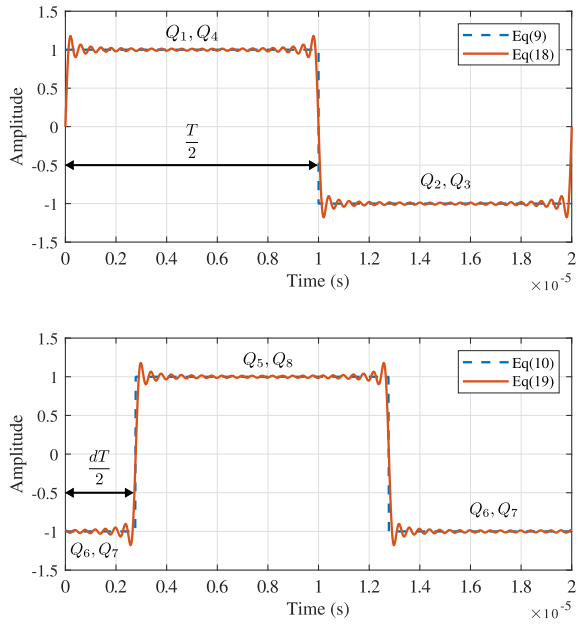

FIGURE 2. Verification of Fourier coefficients, $d = 0.2764$ ($\phi = 0.873$ rad).

$$A'_n = \begin{cases} \frac{-4\sin(n\phi)}{n\pi}, & n \text{ is odd} \\ 0, & n \text{ is even} \end{cases} \tag{16}$$

$$B'_n = \begin{cases} \frac{4\cos(n\phi)}{n\pi}, & n \text{ is odd} \\ 0, & n \text{ is even} \end{cases} \tag{17}$$

where ϕ is the phase shift angle of switching function $S_2(t)$ with respect to $S_1(t)$. The switching functions can, therefore, be represented using (11),

$$S_1(t) = A_0 + \sum_{n=1}^{N} A_n \cos(n\omega_s t) + \sum_{n=1}^{N} B_n \sin(n\omega_s t) \tag{18}$$

$$S_2(t) = A'_0 + \sum_{n=1}^{N} A'_n \cos(n\omega_s t) + \sum_{n=1}^{N} B'_n \sin(n\omega_s t) \tag{19}$$

C. STEP 3: VALIDATION OF FOURIER COEFFICIENTS

Fig. 2 shows the comparison between the piece-wise switching functions, $S_1(t)$ and $S_2(t)$, obtained using (9) and (10) with Fourier switching functions obtained using (18) and (19) for $N = 50$. The Fourier coefficients have been computed correctly.

D. STEP 4: DEFINING THE DAB CONVERTER DYNAMICS

Once the switching functions have been defined and represented correctly, the next step is to define the converter dynamics with the help of state-space equations. The following assumptions have been made:

1) The switching is considered to be instantaneous, and therefore, the effect of dead time has not been considered.
2) The transformer is considered ideal; therefore, the magnetizing inductance is sufficiently large to prevent saturation.
3) All quantities have been referred toward the primary side of the transformer.
4) The input voltage and load dynamics are much slower than the converter's.

The primary side inductor current, $i_L(t)$ and the output capacitor voltage, $v_c(t)$ have been considered as state variables for this model. The primary side inductor current, considering the turn ratio of the transformer N_t, can be expressed as,

$$\frac{di_L(t)}{dt} = \frac{1}{L}\left(V_A(t) - N_t V_B(t) - R_d \cdot i_L(t)\right)$$

where R_d is the lumped resistance that takes into account the equivalent series resistance of the inductor (L) and the on-state resistance of the semiconductor switches.

Similarly, the output capacitor voltage can be expressed as,

$$\frac{dv_c(t)}{dt} = \frac{1}{C_o}\left(i_{rect}(t) - \frac{v_c(t)}{N_t R}\right)$$

where $V_A(t)$ and $V_B(t)$ are the output voltage and input voltage of H-HV and H-LV, respectively, and $i_{rect}(t)$ is the rectified secondary current of the H-LV.

The voltage of the H-bridges, H-HV, and H-LV, as well as the rectified current of H-LV, can now be expressed in terms of the switching functions by using (9) and (10).

$$\frac{di_L(t)}{dt} = \frac{1}{L}\left(S_1(t) \cdot V_{DC} - N_t \cdot S_2(t) \cdot v_c(t) - R_d \cdot i_L(t)\right) \tag{20}$$

Similarly, the output capacitor voltage can be expressed as,

$$\frac{dv_c(t)}{dt} = \frac{1}{C_o}\left(S_2(t) \cdot i_s(t) - \frac{v_c(t)}{N_t R}\right) \tag{21}$$

where $i_s(t)$ is the secondary side input current to H-LV.

E. STEP 5: TRANSITIONING TOWARDS GENERALIZED STATE SPACE AVERAGING

To apply the complex Fourier series, the following changes need to be carried out:

1) The Fourier coefficients computed for the switching functions in Step 2 need to be expressed in terms of equivalent complex Fourier coefficients [29]. Note that the DC component remains independent of this change.

$$\langle S_1 \rangle_0 = A_0 \tag{22}$$

$$\langle S_1 \rangle_{nR} = \frac{A_n}{2} \tag{23}$$

$$\langle S_1 \rangle_{nI} = -\frac{B_n}{2} \tag{24}$$

$$\langle S_2 \rangle_0 = A'_0 \tag{25}$$

$$\langle S_2 \rangle_{nR} = \frac{A'_n}{2} \tag{26}$$

$$\langle S_2 \rangle_{nI} = -\frac{B'_n}{2} \tag{27}$$

where the subscripts R and I denote the real and imaginary components.

2) Equations (20) and (21) need to be decomposed into real and imaginary components.

Therefore, applying (6) and (7) on (20) and (21),

$$\frac{d\langle i_L\rangle_0}{dt} = \frac{1}{L}\left(\langle S_1 \cdot V_{DC}\rangle_0 - N_t \cdot \langle S_2 \cdot v_c\rangle_0 - R_d \cdot \langle i_L\rangle_0\right) \tag{28}$$

$$\frac{d\langle i_L\rangle_{1R}}{dt} = \frac{1}{L}\left(\langle S_1 \cdot V_{DC}\rangle_{1R} - N_t \cdot \langle S_2 \cdot v_c\rangle_{1R} - R_d \cdot \langle i_L\rangle_{1R}\right) + \omega_s\langle i_L\rangle_{1I} \tag{29}$$

$$\frac{d\langle i_L\rangle_{1I}}{dt} = \frac{1}{L}\left(\langle S_1 \cdot V_{DC}\rangle_{1I} - N_t \cdot \langle S_2 \cdot v_c\rangle_{1I} - R_d \cdot \langle i_L\rangle_{1I}\right) - \omega_s\langle i_L\rangle_{1R} \tag{30}$$

$$\frac{d\langle v_c\rangle_0}{dt} = \frac{1}{C_o}\left(\langle S_2 \cdot i_s\rangle_0 - \frac{\langle v_c\rangle_0}{N_t R}\right) \tag{31}$$

$$\frac{d\langle v_c\rangle_{1R}}{dt} = \frac{1}{C_o}\left(\langle S_2 \cdot i_s\rangle_{1R} - \frac{\langle v_c\rangle_{1R}}{N_t R}\right) + \omega_s \cdot \langle v_c\rangle_{1I} \tag{32}$$

$$\frac{d\langle v_c\rangle_{1I}}{dt} = \frac{1}{C_o}\left(\langle S_2 \cdot i_s\rangle_{1I} - \frac{\langle v_c\rangle_{1I}}{N_t R}\right) - \omega_s \cdot \langle v_c\rangle_{1R} \tag{33}$$

Equations (28), (32), and (33) can be truncated based on the fourth assumption. (29)–(31) contains the product of the fundamental harmonics as well as the product of the DC component. Therefore, (8) is necessary to further simplify (29)–(31).

Considering that the $-N^{th}$ coefficient is a complex conjugate of the N^{th} coefficient, we have for $N = 1$,

$$\langle xy\rangle_0 = \langle x\rangle_1 \cdot \langle y\rangle_{-1} + \langle x\rangle_0 \cdot \langle y\rangle_0 + \langle x\rangle_{-1} \cdot \langle y\rangle_1 \tag{34}$$

$$\langle xy\rangle_1 = \langle x\rangle_1 \cdot \langle y\rangle_0 + \langle x\rangle_0 \cdot \langle y\rangle_1 \tag{35}$$

In general, for the first M odd harmonics,

$$\langle xy\rangle_0 = \langle x\rangle_0 \cdot \langle y\rangle_0 + 2 \cdot \left(\sum_{k=1}^{M}(\langle x\rangle_{(2k-1)R} \cdot \langle y\rangle_{(2k-1)R} + \langle x\rangle_{(2k-1)I} \cdot \langle y\rangle_{(2k-1)I})\right) \tag{36}$$

Similarly,

$$\langle xy\rangle_{(2k-1)R} = \langle x\rangle_{(2k-1)R} \cdot \langle y\rangle_0 + \langle x\rangle_0 \cdot \langle y\rangle_{(2k-1)R} \tag{37}$$

$$\langle xy\rangle_{(2k-1)I} = \langle x\rangle_{(2k-1)I} \cdot \langle y\rangle_0 + \langle x\rangle_0 \cdot \langle y\rangle_{(2k-1)I} \tag{38}$$

where $k = 1, 2, 3... M$.

Applying (36)–(38) to (29)–(31), we have,

$$\frac{d\langle i_L\rangle_{1R}}{dt} = \frac{1}{L}\left(\left(\langle S_1\rangle_{1R} \cdot \langle V_{DC}\rangle_0 + \langle S_1\rangle_0 \cdot \langle V_{DC}\rangle_{1R}\right) - N_t \cdot \left(\langle S_2\rangle_{1R} \cdot \langle v_c\rangle_0 + \langle S_2\rangle_0 \cdot \langle v_c\rangle_{1R}\right) - R_d \cdot \langle i_L\rangle_{1R}\right) + \omega_s\langle i_L\rangle_{1I}$$

$$\frac{d\langle i_L\rangle_{1I}}{dt} = \frac{1}{L}\left(\left(\langle S_1\rangle_{1I} \cdot \langle V_{DC}\rangle_0 + \langle S_1\rangle_0 \cdot \langle V_{DC}\rangle_{1I}\right) - N_t \cdot \left(\langle S_2\rangle_{1I} \cdot \langle v_c\rangle_0 + \langle S_2\rangle_0 \cdot \langle v_c\rangle_{1I}\right) - R_d \cdot \langle i_L\rangle_{1I}\right) - \omega_s\langle i_L\rangle_{1R}$$

$$\frac{d\langle v_c\rangle_0}{dt} = \frac{1}{C_o}\left(\langle S_2\rangle_0 \cdot \langle i_L\rangle_0 + 2 \cdot \left(\langle S_2\rangle_{1R} \cdot \langle i_L\rangle_{1R} + \langle S_2\rangle_{1I} \cdot \langle i_L\rangle_{1I}\right) - \frac{\langle v_c\rangle_0}{N_t R}\right)$$

Applying the fourth assumption and substituting the values of $\langle S_1\rangle_0$, $\langle S_1\rangle_{nR}$, $\langle S_1\rangle_{nI}$, $\langle S_2\rangle_0$, $\langle S_2\rangle_{nR}$, and $\langle S_2\rangle_{nI}$ from (22)–(27), we have,

$$\frac{d\langle i_L\rangle_{1R}}{dt} = \frac{1}{L}\left(\frac{2N_t \sin(\phi)\langle v_c\rangle_0}{\pi} - R_d \cdot \langle i_L\rangle_{1R}\right) + \omega_s\langle i_L\rangle_{1I} \tag{39}$$

$$\frac{d\langle i_L\rangle_{1I}}{dt} = \frac{1}{L}\left(\frac{-2V_{DC}}{\pi} + \frac{2N_t \cos(\phi)\langle v_c\rangle_0}{\pi} - R_d \cdot \langle i_L\rangle_{1I}\right) - \omega_s\langle i_L\rangle_{1R} \tag{40}$$

$$\frac{d\langle v_c\rangle_0}{dt} = \frac{1}{C_o}\left(\frac{-4\sin(\phi)\langle i_L\rangle_{1R}}{\pi} - \frac{4\cos(\phi)\langle i_L\rangle_{1I}}{\pi} - \frac{\langle v_c\rangle_0}{N_t R}\right) \tag{41}$$

F. STEP 6: MATRIX REPRESENTATION OF THE SYSTEM

Equations (39), (40), and (41) define the dynamics of the DAB converter by only considering the fundamental component. (42) provides the matrix representation defining the dynamics of the DAB converter, considering only the fundamental component.

$$\frac{d}{dt}\begin{bmatrix} i_{L1R} \\ i_{L1I} \\ v_{c0} \end{bmatrix} = \begin{bmatrix} -\frac{R_d}{L} & \omega_s & \frac{2N_t\sin(\phi)}{\pi L} \\ -\omega_s & -\frac{R_d}{L} & \frac{2N_t\cos(\phi)}{\pi L} \\ \frac{-4\sin(\phi)}{\pi C_o} & \frac{-4\cos(\phi)}{\pi C_o} & \frac{-1}{N_t R C_o} \end{bmatrix}\begin{bmatrix} i_{L1R} \\ i_{L1I} \\ v_{c0} \end{bmatrix} + \begin{bmatrix} 0 & \frac{-2}{L\pi} & 0 \end{bmatrix}^T V_{DC} \tag{42}$$

The system defined by (42) can be easily recomputed to include additional harmonic components using (6)–(8), and (36)–(38) to model the transformer current of the DAB converter accurately. Considering the contribution until the third harmonics, the DAB converter model is described below as an example.

$$\frac{d\langle i_L\rangle_{1R}}{dt} = \frac{1}{L}\left(\frac{2N_t \sin(\phi)\langle v_c\rangle_0}{\pi} - R_d \cdot \langle i_L\rangle_{1R}\right) + \omega_s\langle i_L\rangle_{1I}$$

$$\frac{d\langle i_L\rangle_{1I}}{dt} = \frac{1}{L}\left(\frac{-2V_{DC}}{\pi} + \frac{2N_t \cos(\phi)\langle v_c\rangle_0}{\pi} - R_d \cdot \langle i_L\rangle_{1I}\right) - \omega_s\langle i_L\rangle_{1R}$$

$$\frac{d\langle i_L\rangle_{3R}}{dt} = \frac{1}{L}\left(\frac{2N_t \sin(3\phi)\langle v_c\rangle_0}{3\pi} - R_d \cdot \langle i_L\rangle_{3R}\right) + 3\omega_s\langle i_L\rangle_{3I}$$

TABLE 2. Test Converter Specifications

Parameter	Symbol	Value
Rated Power	P_o	2.5 kW
Input DC Voltage	V_{DC}	500 V
Output DC Voltage	V_o	50 V
Turns Ratio	N_t	10:1
Series Inductance	L	200 μH
Phase Shift Angle	ϕ	0.873 rad
Switching Frequency	f_s	50 kHz
Lumped Resistance	R_d	0.1 Ω
Output Capacitance	C_o	200 μF
Load Resistance	R	1 Ω

$$\frac{d\langle i_L\rangle_{3I}}{dt} = \frac{1}{L}\left(\frac{-2V_{DC}}{3\pi} + \frac{2N_t\cos(3\phi)\langle v_c\rangle_0}{3\pi} - R_d\cdot\langle i_L\rangle_{3I}\right) - 3\omega_s\langle i_L\rangle_{3R}$$

$$\frac{d\langle v_c\rangle_0}{dt} = \frac{1}{C_o}\left(\frac{-4\sin(\phi)\langle i_L\rangle_{1R}}{\pi} - \frac{4\cos(\phi)\langle i_L\rangle_{1I}}{\pi} - \frac{4\sin(3\phi)\langle i_L\rangle_{3R}}{3\pi} - \frac{4\cos(3\phi)\langle i_L\rangle_{3I}}{3\pi} - \frac{\langle v_c\rangle_0}{N_tR}\right)$$

Equation (43) shown at the bottom of this page, showcases the GAM model of the DAB converter considering the first five odd harmonics.

IV. RESULTS AND DISCUSSION

A test case was considered to validate the GAM model. Table 2 showcases the specifications of the DAB converter utilized for the validation purpose. Fig. 3 showcases the experimental setup consisting of a PLECS RT-Box-2 connected to a PC. Table. 3 provides the specifications of the PLECS RT-Box-2. A discretization time step of $T_{disc} = 1.5\,\mu$s was selected for the real-time simulation model.

FIGURE 3. Experimental Setup.

TABLE 3. PLECS RT-Box-2 Specifications [30]

Processor	Xilinx Zynq Ultrascale+	ZU9EG
Number of CPU cores	4	ARM Cortex-A53, 1.5 GHz
Analog inputs	Channels	16
	Resolution	16 bit
	Input type	Differential
	Max. sample rate	5 Msps
Analog outputs	Channels	16
	Resolution	16 bit
	Max. update rate	5 Msps
Digital inputs	Channels	32
	Logic levels	3.3 V (5 V tolerant)
Digital outputs	Channels	32
	Logic levels	3.3 V, 5 V

Fig. 4(a) showcases the steady state output voltage response obtained from GAM ($M = 1$ and $M = 5$), PLECS simulation model, and the RT-Box-2 for the considered test case. While the PLECS model response for the output voltage

$$\frac{d}{dt}\begin{bmatrix} i_{L1R}\\ i_{L1I}\\ i_{L3R}\\ i_{L3I}\\ i_{L5R}\\ i_{L5I}\\ i_{L7R}\\ i_{L7I}\\ i_{L9R}\\ i_{L9I}\\ v_{c0}\end{bmatrix} = \begin{bmatrix} -\frac{R_d}{L} & \omega_s & 0 & 0 & 0 & 0 & 0 & 0 & 0 & 0 & \frac{-N_t\langle S_2\rangle_{1R}}{L}\\ -\omega_s & -\frac{R_d}{L} & 0 & 0 & 0 & 0 & 0 & 0 & 0 & 0 & \frac{-N_t\langle S_2\rangle_{1I}}{L}\\ 0 & 0 & -\frac{R_d}{L} & 3\omega_s & 0 & 0 & 0 & 0 & 0 & 0 & \frac{-N_t\langle S_2\rangle_{3R}}{L}\\ 0 & 0 & -3\omega_s & -\frac{R_d}{L} & 0 & 0 & 0 & 0 & 0 & 0 & \frac{-N_t\langle S_2\rangle_{3I}}{L}\\ 0 & 0 & 0 & 0 & -\frac{R_d}{L} & 5\omega_s & 0 & 0 & 0 & 0 & \frac{-N_t\langle S_2\rangle_{5R}}{L}\\ 0 & 0 & 0 & 0 & -5\omega_s & -\frac{R_d}{L} & 0 & 0 & 0 & 0 & \frac{-N_t\langle S_2\rangle_{5I}}{L}\\ 0 & 0 & 0 & 0 & 0 & 0 & -\frac{R_d}{L} & 7\omega_s & 0 & 0 & \frac{-N_t\langle S_2\rangle_{7R}}{L}\\ 0 & 0 & 0 & 0 & 0 & 0 & -7\omega_s & -\frac{R_d}{L} & 0 & 0 & \frac{-N_t\langle S_2\rangle_{7I}}{L}\\ 0 & 0 & 0 & 0 & 0 & 0 & 0 & 0 & -\frac{R_d}{L} & 9\omega_s & \frac{-N_t\langle S_2\rangle_{9R}}{L}\\ 0 & 0 & 0 & 0 & 0 & 0 & 0 & 0 & -9\omega_s & -\frac{R_d}{L} & \frac{-N_t\langle S_2\rangle_{9I}}{L}\\ \frac{2\langle S_2\rangle_{1R}}{C_o} & \frac{2\langle S_2\rangle_{1I}}{C_o} & \frac{2\langle S_2\rangle_{3R}}{C_o} & \frac{2\langle S_2\rangle_{3I}}{C_o} & \frac{2\langle S_2\rangle_{5R}}{C_o} & \frac{2\langle S_2\rangle_{5I}}{C_o} & \frac{2\langle S_2\rangle_{7R}}{C_o} & \frac{2\langle S_2\rangle_{7I}}{C_o} & \frac{2\langle S_2\rangle_{9R}}{C_o} & \frac{2\langle S_2\rangle_{9I}}{C_o} & \frac{-1}{N_tRC_o}\end{bmatrix}\begin{bmatrix} i_{L1R}\\ i_{L1I}\\ i_{L3R}\\ i_{L3I}\\ i_{L5R}\\ i_{L5I}\\ i_{L7R}\\ i_{L7I}\\ i_{L9R}\\ i_{L9I}\\ v_{c0}\end{bmatrix} + \begin{bmatrix} 0 & \frac{\langle S_1\rangle_{1I}}{L} & 0 & \frac{\langle S_1\rangle_{3I}}{L} & 0 & \frac{\langle S_1\rangle_{5I}}{L} & 0 & \frac{\langle S_1\rangle_{7I}}{L} & 0 & \frac{\langle S_1\rangle_{9I}}{L} & 0\end{bmatrix}^T V_{DC} \quad (43)$$

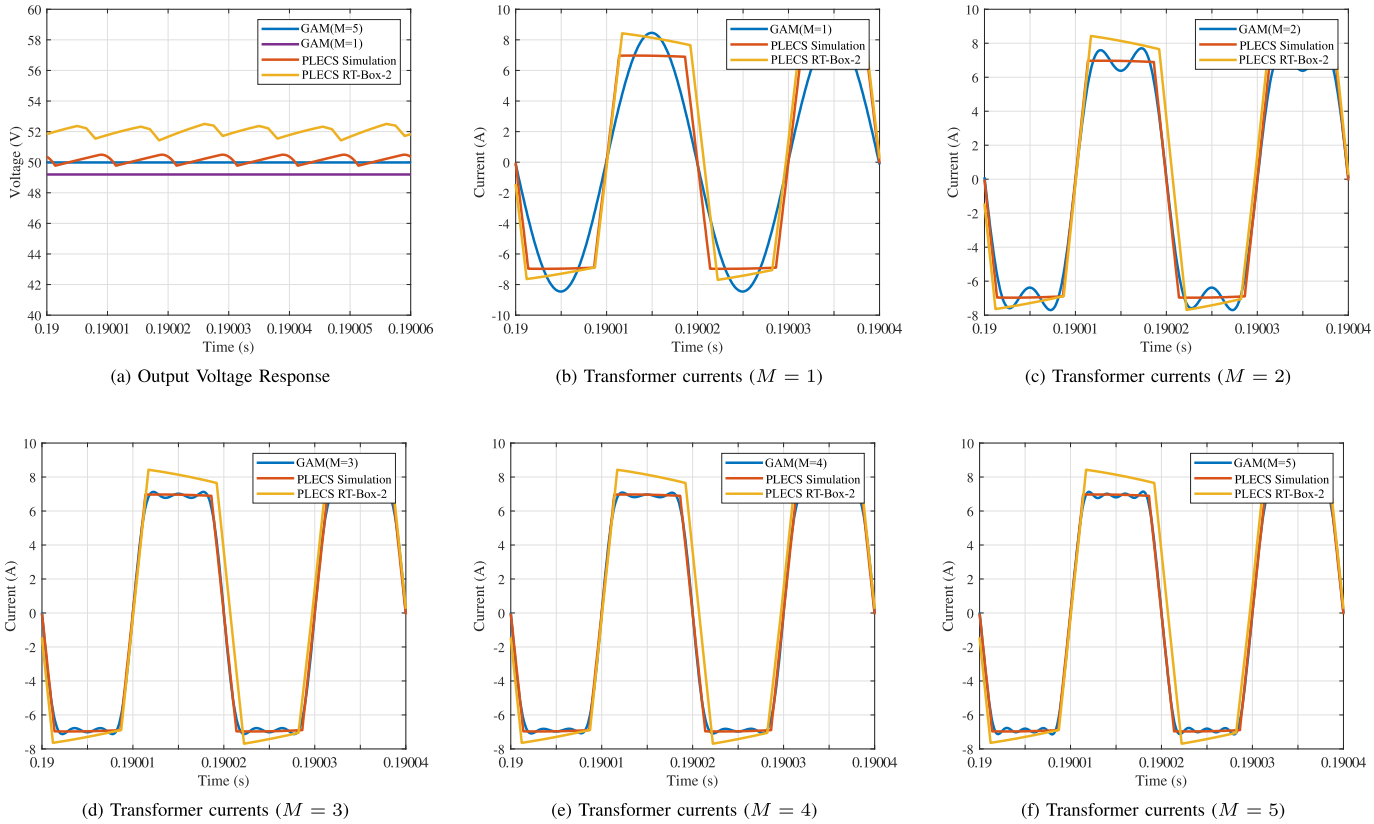

(a) Output Voltage Response (b) Transformer currents ($M = 1$) (c) Transformer currents ($M = 2$)

(d) Transformer currents ($M = 3$) (e) Transformer currents ($M = 4$) (f) Transformer currents ($M = 5$)

FIGURE 4. Comparison of output voltage response and steady-state transformer currents of GAM, PLECS simulation model, and PLECS RT-Box-2 for the first *M* odd harmonics.

contains higher ripple content, the GAM response for the output voltage contains little or no ripple. It is evident from the response that the output voltage of the converter for the case of GAM ($M = 1$) has a steady-state error. On the other hand, the output voltage of GAM ($M = 5$) converges towards the PLECS simulation response such that it is nearly the average of the PLECS simulation response. The real-time simulation response contains a steady-state error but has a similar ripple content to the PLECS simulation model. The transformer current with contributions up to the first M odd harmonics using the GAM can be extracted using the following expression:

$$i_{\mathrm{L}}(t) = 2\sum_{k=1}^{M}\left(i_{\mathrm{L}(2k-1)\mathrm{R}}\cos\left((2k-1)\cdot\left(\omega_{\mathrm{s}}t-\frac{\phi}{2}\right)\right)\right.$$
$$\left.+\, i_{\mathrm{L}(2k-1)\mathrm{I}}\sin\left((2k-1)\cdot\left(\omega_{\mathrm{s}}t-\frac{\phi}{2}\right)\right)\right) \quad (44)$$

With the increase in M, the accuracy of the GAM increases as shown in Fig. 4(b)–(f) that showcases the comparison of the reconstructed transformer currents of the GAM with the response of the PLECS simulation model and the real-time simulation model.

To quantitatively evaluate the accuracy of the GAM obtained using the proposed procedure, several GAMs (fundamental, third, fifth, seventh, and ninth harmonics) are compared against the PLECS and the real-time simulation models. Table 4 showcases the GAM accuracy. All models are operated at five different operating power set-points starting from 0.5 kW up to the rated power of 2.5 kW. Absolute error is calculated by comparing the output power of a given model type with the analytically calculated power, P_{o}. Results indicate that the GAM ($M = 1$) is the most inaccurate model among the considered GAMs with an error of greater than 3% up to a maximum error of 21.16%. As M increases for the subsequent GAMs, this error significantly reduces. The GAM ($M = 5$) presents an error of less than 1% and has relatively higher accuracy than other GAMs, PLECS simulation, and real-time simulation models on the RT-Box-2. It is interesting to note two observations. First, the contribution up to the ninth harmonic ($M = 5$) is sufficient to model the transformer currents of the converter accurately. Second, the

TABLE 4. Evaluation of GAM Accuracy

d	0.0993	0.1486	0.1916	0.2333	0.2764
P_{o}	0.5 kW	1 kW	1.5 kW	2 kW	2.5 kW
Model Type	**% Error**				
PLECS	0.868	0.748	0.631	0.652	0.681
PLECS RT-Box	104.69	9.399	12.909	12.914	8.288
GAM ($M = 1$)	21.16	15.536	11.021	6.932	3.184
GAM ($M = 2$)	5.177	1.331	0.625	1.57	1.662
GAM ($M = 3$)	0.64	1.019	0.975	0.412	0.265
GAM ($M = 4$)	0.733	0.869	0.121	0.355	0.418
GAM ($M = 5$)	0.992	0.380	0.226	0.234	0.065

transformer currents obtained from the real-time simulation present a similar wave shape; however, they contain inaccuracies in their amplitudes. An error of 104.69% was observed for PLECS RT-Box-2 at $P_o = 0.5$ kW. This error reduces significantly as the operating power gradually increases. The following two factors can justify the amplitude inaccuracies throughout the operating power range and the large error at $P_o = 0.5$ kW. First, the RT-Box-2 contains four available FPGA cores; however, only three are available for computation during the real-time simulation. The remaining core is reserved for the Linux operating system, which runs internally. The discretization time step depends not only on the complexity of the real-time simulation model of the power electronics converter but also on the switching frequency. The best time step that could be achieved for RT-Box-2, considering the converter model and choice of switching frequency, was $T_{disc} = 1.5$ μs. Any discretization step below 1.5 μs leads to an over-run condition of the real-time simulator. The computation load distribution among the FPGA cores is inconsistent in this condition. This inconsistency causes overburden on the FPGA cores and causes the converter quantities visualized on the scope to contain frequent fluctuations and inaccuracies. Second, to achieve an operating power of 0.5 kW, the phase angle required is approximately $\phi = 0.312$ rad. This phase angle is expressed as 1.98 μs when translated into the switching period. For the chosen discretization time-step, the FPGA cannot accurately reconstruct the transformer current since the FPGA updates the converter quantities every 1.5 μs. Assuming that $T = 0$ initially, information is lost between T = 1.5 μs and T = 3 μs as the FPGA updates every 1.5 μs. However, this issue no longer exists as the phase angle gradually increases. Considering the operating power of $P_o = 1.5$ kW, the corresponding phase angle is approximately $\phi = 0.602$ rad. This phase angle is expressed as 3.83 μs when translated into the switching period. In this case, the FPGA can reconstruct the transformer currents more accurately than in the previous case, as the data points of the transformer current are retained within two samples of 1.5 μs each. This is evident by the decrease in error for PLECS RT-Box-2 as the operating power increases beyond 0.5 kW.

V. CONCLUSION

DC-DC converters such as a DAB cannot be modeled by considering the small ripple approximation as it contains an intermediate AC stage. As a result, the GAM technique is utilized to capture the contribution of higher-order harmonics. However, the GAM technique is often restricted to considering only the fundamental frequency leading to a sinusoidal current, which presents an inaccurate representation of the DAB transformer current. In this paper, a step-by-step procedure to obtain a DAB model with the help of the GAM technique using only Fourier transformations was proposed. Unlike the conventional GAM technique, which is often restricted to consideration of only the fundamental component, the proposed procedure provides general expressions that can be used for developing the GAM of the converter that can take into account higher-order harmonics. Moreover, the impact of the transformer's turn ratio was considered within the modeling procedure. The fundamental GAM ($M = 1$) of the DAB converter was developed to describe the modeling procedure and extended further to develop a ninth harmonic GAM ($M = 5$) of the converter. The validation of the model obtained with the proposed method was carried out by comparing transformer currents obtained from several GAMs (fundamental, third, fifth, seventh, and ninth harmonics) against the transformer currents of the simulation model and real-time simulation model in PLECS and PLECS RT-Box-2, respectively. The steady-state output voltage was evaluated by comparing the PLECS simulation and real-time simulation response with GAM ($M = 1$ and $M = 5$). A quantitative evaluation of model accuracy indicated that the ninth harmonic GAM of the converter was more consistent in accuracy over the operating power range than the PLECS simulation and the real-time simulation model on the PLECS RT-Box-2.

REFERENCES

[1] S. Bacha et al., *Power Electronic Converters Modeling and Control*, (Advanced Textbooks in Control and Signal Processing Series), vol. 454. New York City, NY, USA: Springer, 2014.

[2] R. W. d. Doncker, "Power conversion apparatus for DC/DC conversion using dual active bridges," U. S. Patent 5027264A, Jun. 25, 1991.

[3] B. Zhao, Q. Song, W. Liu, and Y. Xiao, "Next-generation multifunctional modular intelligent UPS system for smart grid," *IEEE Trans. Ind. Electron.*, vol. 60, no. 9, pp. 3602–3618, Sep. 2013.

[4] H. Wen, W. Xiao, and B. Su, "Nonactive power loss minimization in a bidirectional isolated DC–DC converter for distributed power systems," *IEEE Trans. Ind. Electron.*, vol. 61, no. 12, pp. 6822–6831, Dec. 2014.

[5] B. Zhao, Q. Song, and W. Liu, "Experimental comparison of isolated bidirectional DC–DC converters based on all-si and all-sic power devices for next-generation power conversion application," *IEEE Trans. Ind. Electron.*, vol. 61, no. 3, pp. 1389–1393, Mar. 2013.

[6] S. P. Engel, M. Stieneker, N. Soltau, S. Rabiee, H. Stagge, and R. W. D. Doncker, "Comparison of the modular multilevel DC converter and the dual-active bridge converter for power conversion in HVDC and MVDC grids," *IEEE Trans. Power Electron.*, vol. 30, no. 1, pp. 124–137, Jan. 2015.

[7] N. Hou and Y. W. Li, "A tunable power sharing control scheme for the output-series DAB DC–DC system with independent or common input terminals," *IEEE Trans. Power Electron.*, vol. 34, no. 10, pp. 9386–9391, Oct. 2019.

[8] B. Zhao, Q. Song, J. Li, Y. Wang, and W. Liu, "High-frequency-link modulation methodology of DC–DC transformer based on modular multilevel converter for HVDC application: Comprehensive analysis and experimental verification," *IEEE Trans. Power Electron.*, vol. 32, no. 5, pp. 3413–3424, May 2017.

[9] F. D. Freijedo, E. Rodriguez-Diaz, and D. Dujic, "Stable and passive high-power dual active bridge converters interfacing MVDC grids," *IEEE Trans. Ind. Electron.*, vol. 65, no. 12, pp. 9561–9570, Dec. 2018.

[10] J. Shi, W. Gou, H. Yuan, T. Zhao, and A. Q. Huang, "Research on voltage and power balance control for cascaded modular solid-state transformer," *IEEE Trans. Power Electron.*, vol. 26, no. 4, pp. 1154–1166, Apr. 2011.

[11] T. Zhao, G. Wang, S. Bhattacharya, and A. Q. Huang, "Voltage and power balance control for a cascaded H-bridge converter-based solid-state transformer," *IEEE Trans. Power Electron.*, vol. 28, no. 4, pp. 1523–1532, Apr. 2013.

[12] X. She, A. Q. Huang, and X. Ni, "Current sensorless power balance strategy for DC/DC converters in a cascaded multilevel converter based solid state transformer," *IEEE Trans. Power Electron.*, vol. 29, no. 1, pp. 17–22, Jan. 2014.

[13] J. Everts, F. Krismer, J. V. d. Keybus, J. Driesen, and J. W. Kolar, "Charge-based ZVS soft switching analysis of a single-stage dual active bridge AC-DC converter," in *Proc. IEEE Energy Convers. Congr. Expo.*, 2013, pp. 4820–4829.

[14] L. Xue, Z. Shen, D. Boroyevich, P. Mattavelli, and D. Diaz, "Dual active bridge-based battery charger for plug-in hybrid electric vehicle with charging current containing low frequency ripple," *IEEE Trans. Power Electron.*, vol. 30, no. 12, pp. 7299–7307, Dec. 2015.
[15] J. Everts, F. Krismer, J. V. d. Keybus, J. Driesen, and J. W. Kolar, "Optimal ZVS modulation of single-phase single-stage bidirectional DAB AC–DC converters," *IEEE Trans. Power Electron.*, vol. 29, no. 8, pp. 3954–3970, Aug. 2014.
[16] N. M. L. Tan, T. Abe, and H. Akagi, "Design and performance of a bidirectional isolated DC–DC converter for a battery energy storage system," *IEEE Trans. Power Electron.*, vol. 27, no. 3, pp. 1237–1248, Mar. 2012.
[17] F. Xue, R. Yu, and A. Q. Huang, "A 98.3% efficient GaN isolated bidirectional DC–DC converter for DC microgrid energy storage system applications," *IEEE Trans. Ind. Electron.*, vol. 64, no. 11, pp. 9094–9103, Nov. 2017.
[18] V. Karthikeyan and R. Gupta, "Multiple-input configuration of isolated bidirectional DC–DC converter for power flow control in combinational battery storage," *IEEE Trans. Ind. Inform.*, vol. 14, no. 1, pp. 2–11, Jan. 2018.
[19] R. Naayagi, A. Forsyth, and R. Shuttleworth, "Bidirectional control of a dual active bridge DC–DC converter for aerospace applications," *IET Power Electron.*, vol. 5, no. 7, pp. 1104–1118, 2012.
[20] G. Buticchi, D. Barater, L. F. Costa, and M. Liserre, "A PV-inspired low-common-mode dual-active-bridge converter for aerospace applications," *IEEE Trans. Power Electron.*, vol. 33, no. 12, pp. 10467–10477, Dec. 2018.
[21] R. S. Deshmukh, G. Rituraj, H. Vahedi, A. Shekhar, and P. Bauer, "Impact of electrolyzer on the operation of a dual active bridge converter," in *Proc. IEEE 49th Annu. Conf. IEEE Ind. Electron. Soc.*, 2023, pp. 1–6.
[22] R. S. Deshmukh, G. Rituraj, N. Lock, H. Vahedi, A. Shekhar, and P. Bauer, "Implementation of real-time digital twin of dual active bridge converter in electrolyzer applications," in *Proc. IEEE 49th Annu. Conf. IEEE Ind. Electron. Soc.*, 2023, pp. 1–6.
[23] F. Krismer and J. W. Kolar, "Accurate small-signal model for the digital control of an automotive bidirectional dual active bridge," *IEEE Trans. Power Electron.*, vol. 24, no. 12, pp. 2756–2768, Dec. 2009.
[24] H. Qin and J. W. Kimball, "Generalized average modeling of dual active bridge DC–DC converter," *IEEE Trans. Power Electron.*, vol. 27, no. 4, pp. 2078–2084, Apr. 2012.
[25] J. A. Mueller and J. W. Kimball, "An improved generalized average model of DC–DC dual active bridge converters," *IEEE Trans. Power Electron.*, vol. 33, no. 11, pp. 9975–9988, Nov. 2018.
[26] S. Ghosh, D. Das, B. Singh, S. Janardhanan, and S. Mishra, "Frequency-domain modeling of dual-active-bridge converter based on harmonic balance approach," *IEEE J. Emerg. Sel. Topics Ind. Electron.*, vol. 3, no. 1, pp. 166–176, Jan. 2020.
[27] J. A. Mueller and J. W. Kimball, "Modeling dual active bridge converters in DC distribution systems," *IEEE Trans. Power Electron.*, vol. 34, no. 6, pp. 5867–5879, Jun. 2019.
[28] S. R. Sanders, J. M. Noworolski, X. Z. Liu, and G. C. Verghese, "Generalized averaging method for power conversion circuits," *IEEE Trans. power Electron.*, vol. 6, no. 2, pp. 251–259, Apr. 1991.
[29] W. Foundation, "Fourier series." [Online]. Available: https://en.wikipedia.org/wiki/Fourier_series
[30] Plexim, "Rt-box 2." [Online]. Available: https://www.plexim.com/products/rt_box/rt_box_2

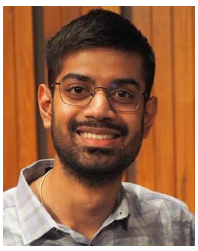

ROHAN SHAILESH DESHMUKH (Graduate Student Member, IEEE) received the B.E. degree in electrical engineering from the Babaria Institute of Technology, Vadodara, India, in 2018, and the M.Sc. degree in electrical power engineering from Delft University of Technology, Delft, The Netherlands, in 2021. He is working toward the Ph.D. degree with the DC Systems, Energy Conversion and Storage Research Group, Delft University of Technology, Delft, The Netherlands. His research interests include designing, modeling, and controlling power electronics converters for high-power electrolysis systems.

PAVOL BAUER (Senior Member, IEEE) received the master's degree in electrical engineering from the Technical University of Kosice, Kosice, Slovakia, in 1985, and the Ph.D. from the Delft University of Technology, Delft, The Netherlands, in 1995. From 2002 to 2003, he was with KEMA (DNVGL), Arnhem, The Netherlands, on different projects related to power electronics applications in power systems. He is currently a Full Professor with the Department of Electrical Sustainable Energy, Delft University of Technology, and the Head of DC Systems, Energy Conversion, and Storage Group. He is also a Professor with the Brno University of Technology, Brno, Czech Republic, and an Honorary Professor with the Politehnica University Timişoara, Timişoara, Romania. He has authored or coauthored more than 120 journal articles and 500 conference papers in his field. He is an author or co-author of eight books, holds seven international patents, and organized several tutorials at international conferences. He has worked on many projects for the industry concerning wind and wave energy, power electronic applications for power systems such as Smarttrafo, HVDC systems, projects for smart cities such as photovoltaic (PV) charging of electric vehicles, PV and storage integration, contactless charging, and he participated in several Leonardo da Vinci and H2020, and Electric Mobility Europe EU projects as a Project Partner (ELINA, INETELE, E-Pragmatic, Micact, Trolley 2.0, OSCD, P2P, and Progressus) and a Coordinator (PEMCWebLab.com-Edipe, SustEner, Eranet DCMICRO). Prof. Bauer is the Former Chairman of the Benelux IEEE Joint Industry Applications Society, Power Electronics and Power Engineering Society Chapter, the Chairman of the Power Electronics and Motion Control Council, a Member of the Executive Committee of the European Power Electronics Association, and also a Member of the International Steering Committee at numerous conferences.

HANI VAHEDI (Senior Member, IEEE) received the Ph.D. degree (with Hons.) from École de Technologie Superieure (ÉTS), University of Quebec, Quebec, QC, Canada, in 2016. He is the Inventor of the PUC5 converter, holds multiple U.S./world patents, and transferred that technology to the industry, where he developed the first bidirectional electric vehicle DC charger based on his invention. After seven years of experience in industry as a Power Electronics Designer and Chief Scientific Officer, he joined the Delft University of Technology, Delft, The Netherlands, where he is currently an Assistant Professor at the DCE&S Group, working toward the electrification of industrial processes for clean energy transition. He has authored or coauthored more than 60 technical papers in IEEE conferences and Transactions. He also authored or coauthored a book on Springer Nature and a book chapter in Elsevier. His research interests include multilevel converter topologies, control and modulation techniques, and their applications in the electrification of industrial processes and clean energy transition, such as smart grids, renewable energy conversion, electric vehicle chargers, green hydrogen production (electrolyzers), and fuel-cell systems. He was the recipient of the Best Ph.D. Thesis Award from ETS for the academic year of 2016–2017. He is an active member of the IEEE Industrial Electronics Society (IES) and its Student & Young Professionals (S&YP) committee. He is the Co-chair of special sessions, Co-organizer of the S&YP Forum, and Co-chair of 3M video sessions in IES conferences. He is also an Associate Editor for IEEE TRANSACTIONS ON INDUSTRIAL ELECTRONICS and IEEE OPEN JOURNAL OF INDUSTRIAL ELECTRONICS SOCIETY.